Supporting Information

Silicon Carbide Single Crystal for High-Temperature Supercapacitors

Chang Liang[a, b], Shouzhi Wang*[a, b], Ge Tian[c], Songyang Lv[b], Guodong Wang[b], Xuejian Xie*[b], Lili Li[b], Xiangang Xu[b], Guangxia Liu[d] and Lei Zhang*[a, b]

[a] Shenzhen Research Institute, Shandong University, Shenzhen, 518000, P. R. China

[b] Institute of Novel Semiconductors, State Key Lab of Crystal Materials, Shandong University, Jinan, 250100, P. R. China.

[c] School of Life Sciences, Shandong First Medical University & Shandong Academy of Medical Sciences, Taian, Shandong 271000, China

[d] Municipal and Equipment Engineering Department, Shandong Urban Construction Vocational College, Jinan, 250103 P. R. China.

*E-mail: wangsz@sdu.edu.cn; xiexj@sdu.edu.cn; leizhang528@sdu.edu.cn;

This file includes:

S1. Materials

S2. Experimental Section

S3. Characterization Methods

S4. Electrochemical Measurements.

S5. Supplementary Figures S1–S17

S6. Table S1

S1. Materials

Reagents were purchased from Sinopharm Chemical Reagent Co., Ltd. (Shanghai). All the reagents were used as received.

S2. Experimental Section

S2.1 reparation of Porous N-type SiC crystal electrode

4-inch N-type SiC ingots are grown by physical vapor transport. The resulting ingots are processed into wafers by a cutting process. After grinding and polishing treatment, so that its surface is transparent and scratch-free. The wafer is then processed into 1×1.5 cm wafers by laser cutting. The porous N-type SiC electrode material was prepared by the improved electrochemical oxidation process. Specifically, two different etching solutions are applied as a two-electrode system of electrolytes. SiC crystal and platinum wire serve as anode and cathode, respectively. First of all, the first etching solution is saturated ammonium bifluoride solution. The etching voltage is constant at 18 V for 10 min to ensure that the surface surface layer is uniformly and large-area shed. In the second step, the configured etching solution (volume ratio $C_2H_5OH:HF:H_2O_2=6:3:1$) is replaced and the voltage is converted to 20 V for 20, 25, and 30 min, respectively.

During electrochemical anodizing, the silicon and carbon atoms in the N-type SiC single crystal begin to lose electrons and undergo oxidation reactions. This causes the atoms or ions on the surface of the SiC to oxidize and dissolve, which in turn forms initial holes or pits. As the reaction progresses, the pores or pits gradually widen and deepen, forming a highly ordered porous structure.

S2.2 SiC ionic-liquid-based supercapacitor (IL-based SC) design

According to the different electrochemical etching times of N-type SiC crystals, a series of porous SiC electrode materials were prepared. The time is 0, 20, 25, 30min, and it is labeled SiC-raw, SiC-1, SiC-2 and I SiC-3 respectively. For the experimentally obtained samples, they are washed in vacuum oven with absolute ethanol and deionized water and dried to 60 °C. Finally, porous SiC single crystal products are obtained.

SiC-based IL SC is assembled in an argon-filled glove box (< 0.01 ppm of oxygen and water). The porous SiC-2 material is used as the anode and cathode, respectively,

and the 1-ethyl 1-3 methimidazole (trifluoromethyl sulfonyl) imide (EMImNTf$_2$) used as electrolyte.

S2.3 Theoretical calculation method:

The present calculations were carried out by Vienna Ab initio Simulation Package (VASP) [1,2] implementation of DFT in conjunction with the projector augmented wave (PAW) formalism. Consequently, the H $1s^1$, C $2s^22p^2$, N $2s^22p^3$, O $2s^22p^4$, F $2s^22p^5$, S $3s^23p^4$, and Si $2s^22p^2$ states are treated as valence electrons. The electronic wave functions are expanded in plane waves using an energy cut off of 500 eV. The convergence criteria of force and energy for the structural relaxation were set at 0.01 eV/Å and 10^{-5} eV. The lattice parameters of primitive hexagonal 4H-SiC were a=b=3.09 Å, c=15.16 Å after optimization. Then we constructed the 4x2x1 supercells to simulate a system with increased nitrogen doping concentrations (N$_C$@SiC), as shown in **Figure S15(b-d)**. The electron exchange and correlation (XC) of the generalized gradient approximation (GGA) functional of Perdew, Burke, and Ernzerhof (PBE) was used to optimize the configurations [3]. Monkhorst-Pack k-points [6] were sampled using a 4x4x4 for the relaxation and total energy and electronic calculations.

To determine the optimal adsorption surface for C$_6$H$_{11}$N$_2$•C$_2$F$_6$NO$_4$S$_2$ (NFT2) on SiC surface, we first constructed SiC-001 surfaces that exposed Si and C, respectively in **Figure S2**. The thickness of vacuum spacing was ~15Å in the z-direction to prevent spurious interactions. For SiC-001 surfaces, surface energies exposing Si and C are -13.67 and -14.21 eV, respectively. Thus, we constructed a series of NFT2 adsorption models based on the stable SiC-001 surface with exposing C atoms. According to the experiment, we chose the N$_C$@SiC system with the highest N doping concentration, and also constructed the N$_C$@SiC-001 surface with exposing Si and C atoms. The energies of N$_C$@SiC-001 surface are -13.70 eV and -14.33 eV, respectively, as shown in **Figure S16c and S16d**. Thus, a series of models for NFT2 adsorption, were constructed on the stable N$_C$@SiC-001 surface with exposing C atoms.

Each adsorption model are allowed to interact with C$_6$H$_{11}$N$_2$•C$_2$F$_6$NO$_4$S$_2$ (NFT2) and the adsorption energy (E_{ad}) for species X is defined as follows:

$$E_{ad} = E(\text{surface/X}) - E(\text{surface}) - E(\text{X}) \qquad (1)$$

where E(surface/X) is the total energy of the fully relaxed surface/adsorbate system, E(surface) is the total energy of the relaxed substrate slab, and E(X) is the total energy of a free adsorbate species (NFT2). Negative adsorption energy means effective adsorbate binding.

S3. Characterization Methods

The morphology of the as-collected samples was characterized by investigated by SEM (Hitachi S-4800), TEM (Philips Tecnai 20U-Twin), HRTEM (JEM 2100F). The crystal structures were obtained by XRD (Bruker diffractometer D8 Advance, Ni Kα radiation, λ = 1.5418 Å), XPS (Thermo ESCALAB 250 Al Kα radiation, 1486.8 eV), BET (ASAP 2020 sorptometer), PSD (BJH desorption dV/dlog(r) plot volume), Raman (Horiba Jobin Yvon with Ar$^+$ laser 532 nm), EPR (Bruker, A300-10/12), TGA (Hitachi TG/DTA7200), FTIR (Thermo Scientific Nicolet iS20)

S4. Electrochemical Measurements.

Electrochemical performance testing using CHI660E electrochemical workstations. For a three-electrode test system with SiC sample as the working electrode, mercury sulfate was used as the reference electrode and the metal platinum plate was used as the counter electrode in 2 M H_2SO_4 aqueous solution. GCD curves were performed at –0.1 V to –0.8 V at 25 °C. CV curves are performed at –0.1 V to –0.75 V at 25 °C. In two-electrode measurements, CV and GCD test data are collected in the 0-1.0V range from 25°C to 150°C. The alternating current (AC) EIS spectrum was acquired range from 10^{-2} Hz to 10^5 Hz at an open circuit voltage with an AC amplitude of 0.005 V. Mott-Schottky (M-S) for the measured frequency of 973Hz.

The area specific capacity of the electrodes in three-electrode test system, is derived from the GCD curve, calculated according to equation 1.

$$C = \frac{I\Delta t}{S\Delta V} \qquad (2)$$

Where C is the specific capacitance (F cm^{-2}) base on the area of the electrode materials, I is the discharge current (A), Δt is the discharge time (s), S is the area (cm^2) of the active materials of the single electrode, ΔV is the working voltage window (V).

The area specific capacitance for SiC-2 based SC with ILs as electrolyte is calculated from equation 2

$$C = \frac{I\Delta t}{S\Delta V}$$ (2)

Where C is the area specific capacitance (F cm^{-2}) of the device, I is the discharge current (A), Δt is the discharge time (s), S is the total area (cm^2) of active material on the SC, ΔV is the working voltage window (V).

The energy density of the SCs are calculated by equation 3

$$E = \frac{1}{2}C\Delta V^2$$ (3)

Where E is the energy density (mWh cm^{-2}) of the device, C is the area specific capacitance (mF cm^{-2}) of the device, ΔV is the working voltage window (V).

The power density of the SCs are calculated by equation 4

$$P = \frac{E}{\Delta t}$$ (4)

Where P is the power density (mW cm^{-2}) of the device, E is the energy density (mWh cm^{-2}), Δt is the discharge time (s).

According to the M-S theory, the calculated electron concentration, was derived from equation 5

$$\frac{1}{C_s^2} = \frac{2}{(\varepsilon\varepsilon_0 e_0 N_d)}(U - U_{fb} - \frac{\kappa_B T}{e_0})$$ (5)

Where C_s is the space charge capacitance per unit area (F cm^{-2}), N_d is the electron concentration (cm^{-3}), ε is the dielectric constant, ε_0 is the permittivity of vacuum (F m^{-1}), e_0 is the electron charge (C), U is the applied potential (V), U_{fb} is the flat band potential (V), T is the temperature (K), and κ_B is the Boltzmann constant (J K^{-1}).

S5. Supplementary Figures S1–S16
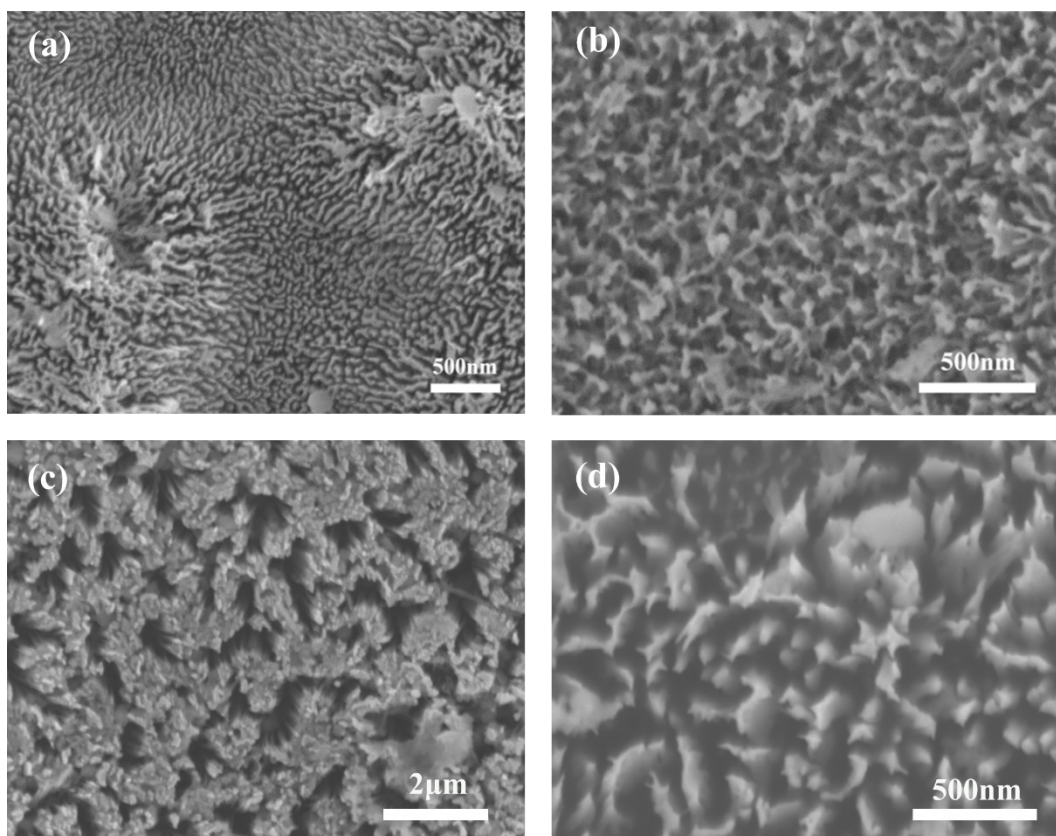
Figure S1. The SEM image of (a) the porous SiC-1 (20min), (b) the porous SiC-3 (30min) and (c,d) the porous SiC−2 after stability test.

Element	Atomic (%)	Mass (%)
Si K	67.73	82.44
C K	27.31	14.21
O K	3.76	2.61
N K	1.20	0.74
Total	100.00	100.00

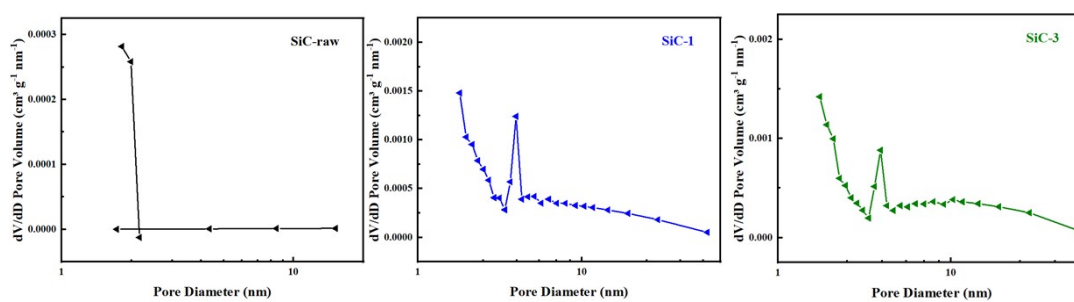**Figure S2:** The EDS result of the SiC-2 heterostructure.

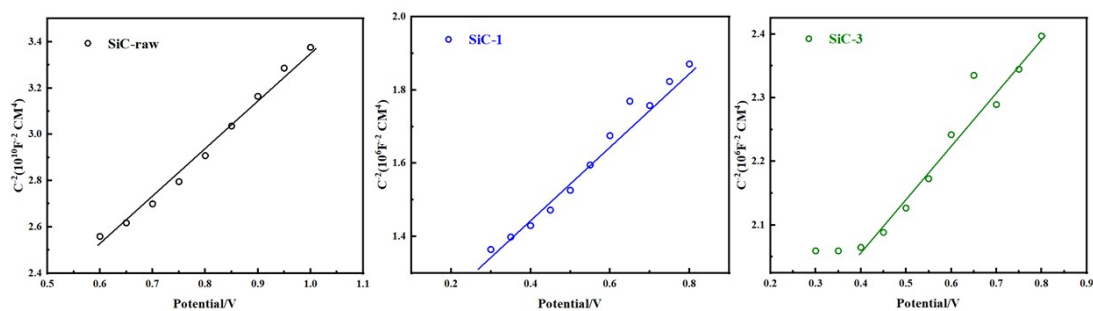**Figure S3.** The pore size distribution plots of SiC-raw, SiC-1 and SiC-3.

Figure S4. The M–S curve of SiC-raw, SiC-1 and SiC-3.
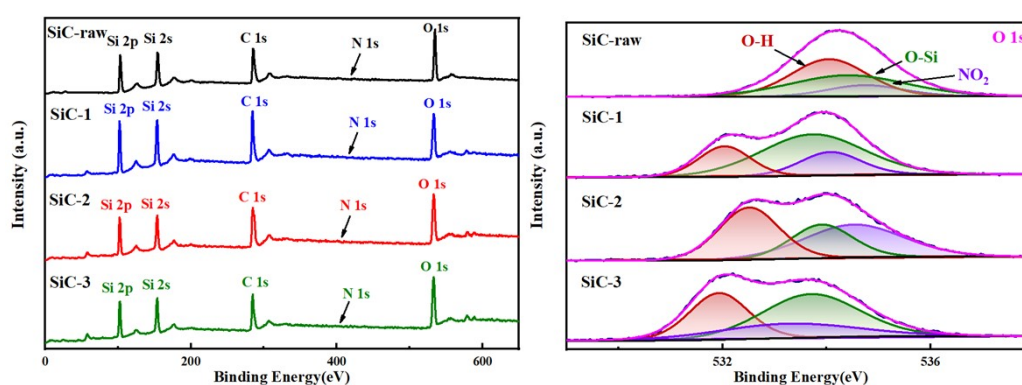
Figure S5. The XPS survey spectra and the high-resolution O 1s XPS spectra.
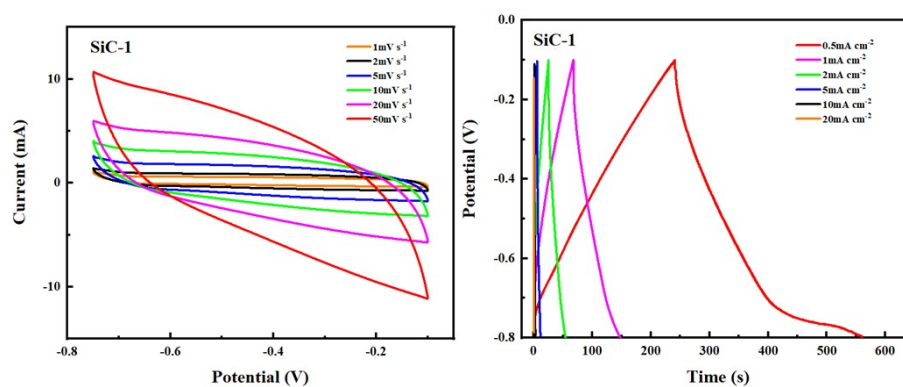
Figure S6. Three-electrode electrochemical performance of SiC-1; the CV curves and the GCD curves.
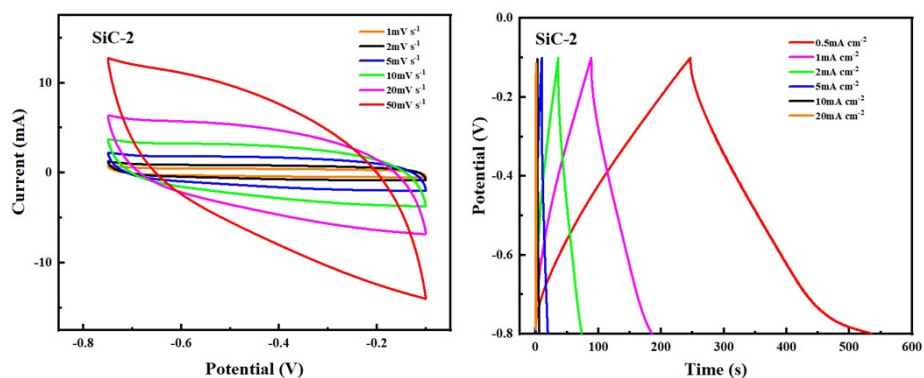
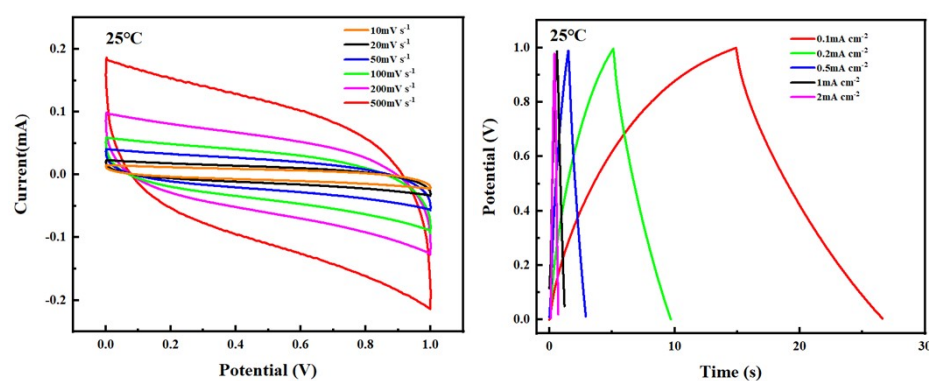**Figure S7.** Three-electrode electrochemical performance of SiC-2; the CV curves and the GCD curves.
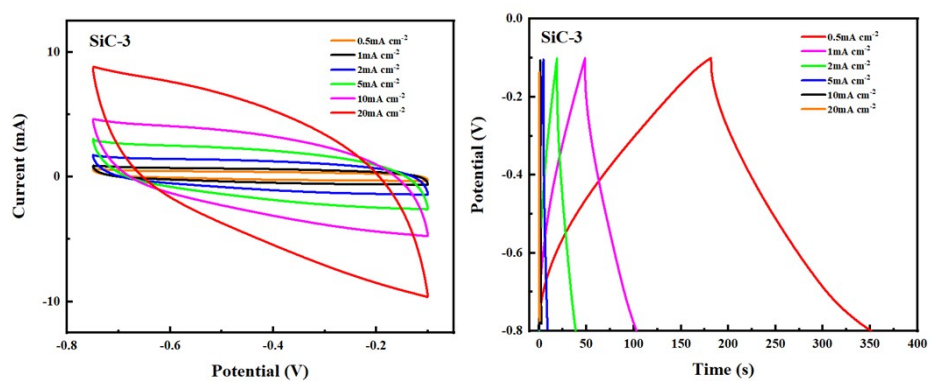
Figure S8. Three-electrode electrochemical performance of SiC-3; the CV curves and the GCD curves.

Figure S9. The electrochemical performance of the SiC IL-based SCs at 25 °C; the CV curves and the GCD curves.
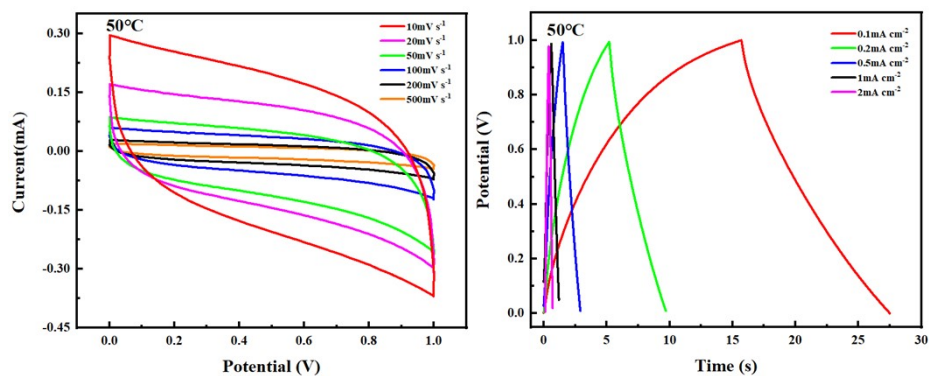
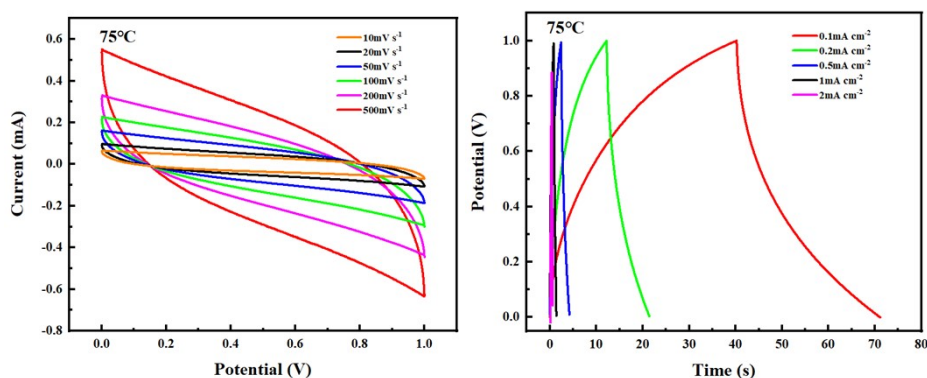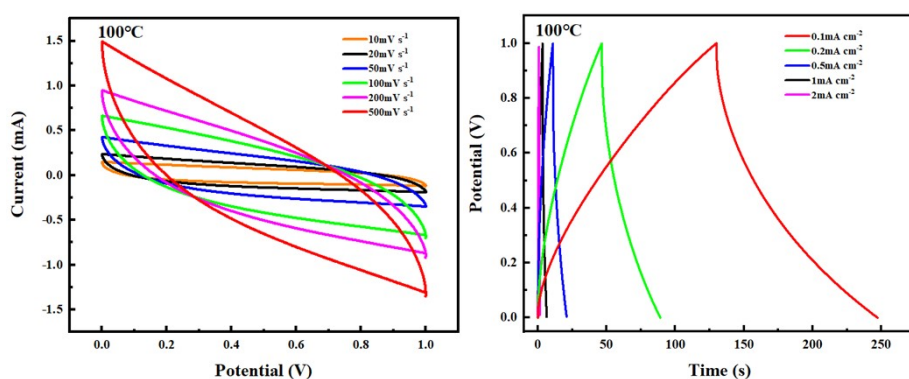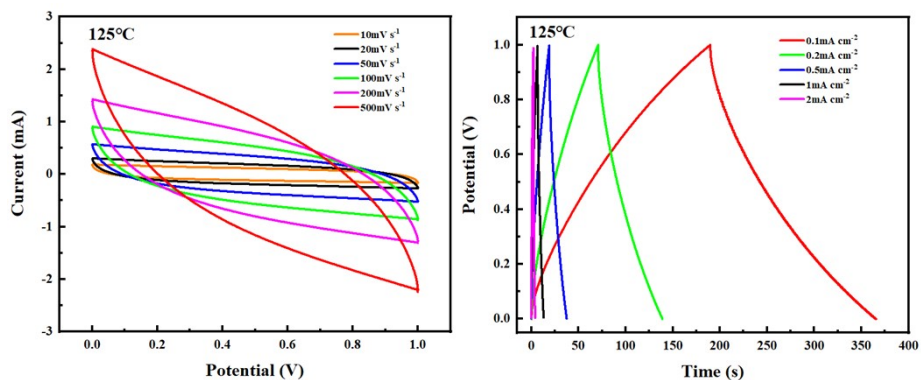**Figure S10.** The electrochemical performance of the SiC IL-based SCs at 50 °C; the CV curves and the GCD curves.

Figure S11. The electrochemical performance of the SiC IL-based SCs at 75 °C; the CV curves and the GCD curves.

Figure S12. The electrochemical performance of the SiC IL-based SCs at 100 °C; the CV curves and the GCD curves.

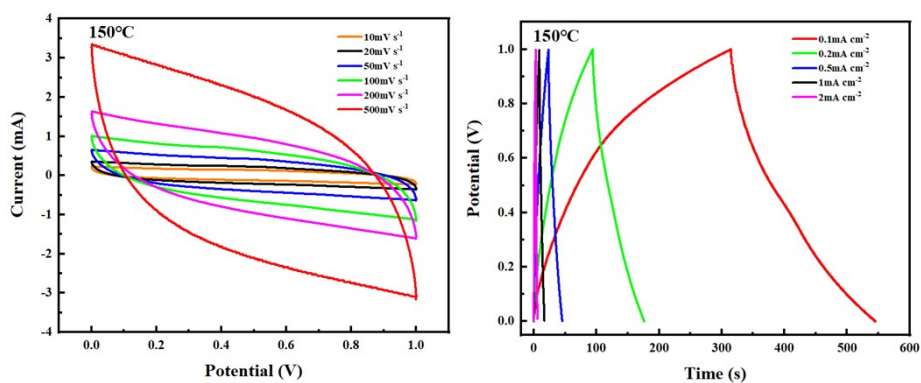**Figure S13.** The electrochemical performance of the SiC IL-based SCs at 125 °C; the CV curves and the GCD curves.

Figure S14. The electrochemical performance of the SiC IL-based SCs at 150 °C; the CV curves and the GCD curves.
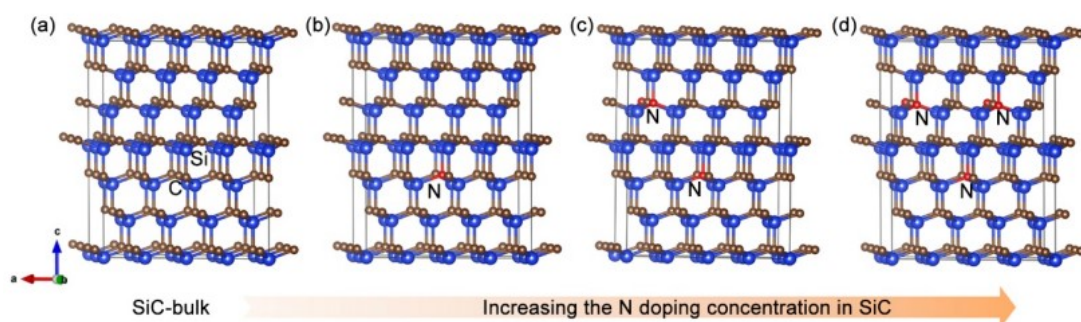

Figure S15. The optimized structures of (a) SiC bulk and (b-d) the $N_C@$ SiC with increased nitrogen doping concentrations.
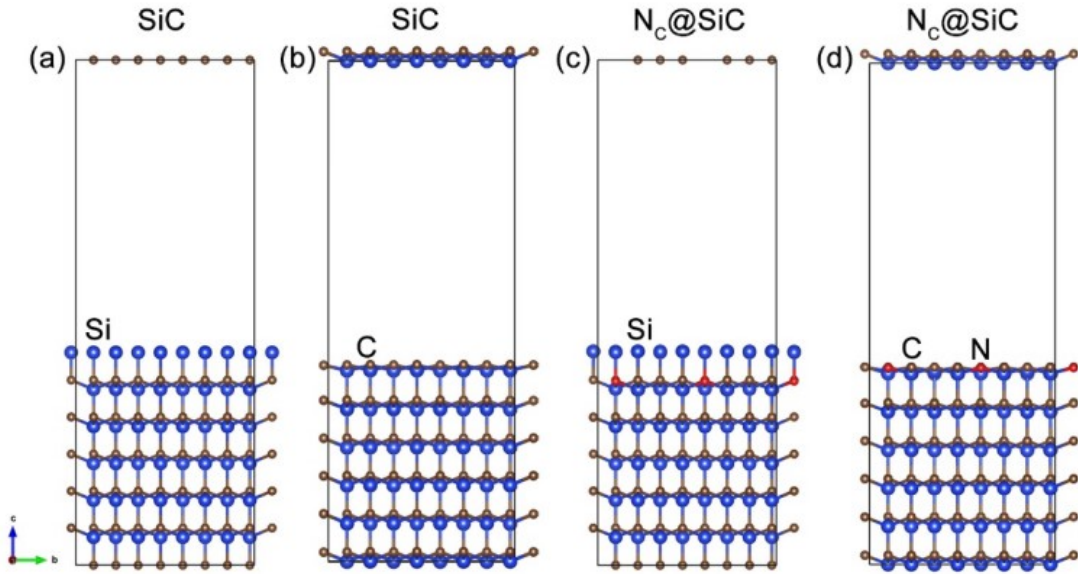
Figure S16. Side view of (a-b) SiC-001 and (c-d) $N_C@$ SiC-001 surface with exposing
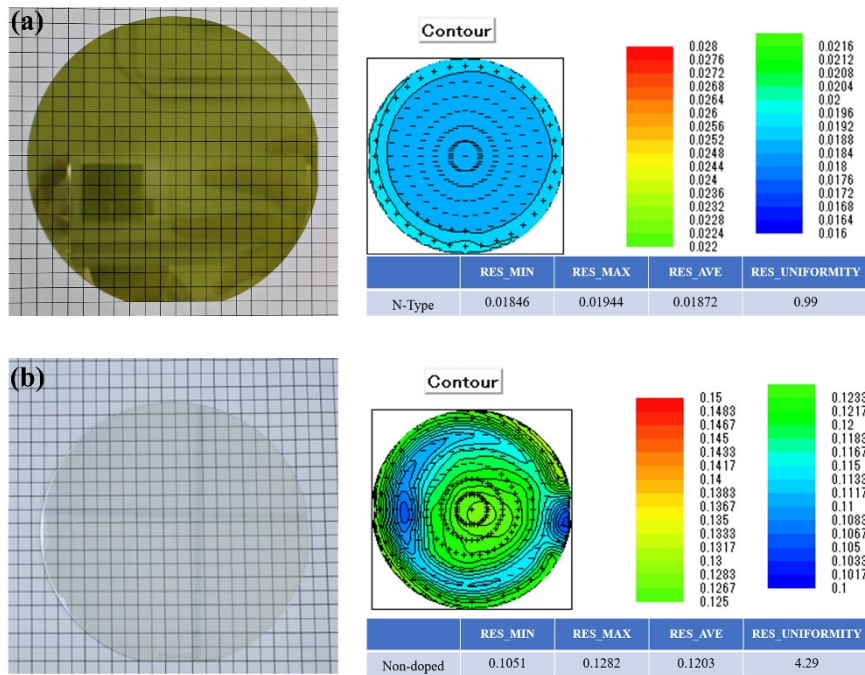
Si and C atoms.

Figure S17. (a) N-type 4-inch SiC wafer and resistivity test data; (b) Non-doped 4-inch

SiC wafer and resistivity test data.

S6. Table S1

Material	Capacitance	Capacity retention	Power density	Energy density	Ref.
SiC nanowires	240 μF cm^{-2}	95% after 20,000 cycles	40 μW cm^{-2}	41 μJ cm^{-2}	*J. Power Sources*, 2013, **230**, 298–302.
SiC nanowires	23mF cm^{-2}	90% after 100,000 cycles	12 mW cm^{-2}	1.7 mJ cm^{-2}	*J. Power Sources*, 2013, **243**, 648–653.
3C-SiC nanowire films	25.6 mF cm^{-2}	100% after 2000 cycles	–	–	*J. Alloys Compd.*, 2014, **605**, 168–172.
SiC nanowires	46.7 mF cm^{-2}	100% after 1000 cycles	–	–	*J. Alloys Compd.*, 2020, **827**, 154168.
SiC@PEDOT	26.53 mF cm^{-2}	104% after 10,000 cycles	–	–	*J. Energy Chem.*, 2022, **66**, 30–37.
SiC microspheres	253.7 F g^{-1}	87.9% rate performance from 5 to 500 mV s^{-1}	–	–	45 *J. Power Sources*, 2015, **282**, 277–285.
SiC wafers	203.7 F g^{-1}	87.3% rate performance from 5 to 500 mV s^{-1}	–	–	*J. Power Sources*, 2016, **307**, 715–723.

References

[1] Kresse, G., Furthmüller, J. Effificient iterative schemes for ab initio total energy calculations using a plane-wave basis set. *Phys. Rev. B* **54**, 11169-11186 (1996).

[2] Kresse, G., Joubert, D. From ultrasoft pseudopotentials to the projector augmented-wave method. *Phys. Rev. B* **59**, 1758-1775 (1999).

[3] Perdew, J. P., Burke, K., Ernzerhof, M. Generalized gradient approximation made simple. *Phys. Rev. Lett.* **77**, 3865-3868 (1996).

[4] Heyd, J., Scuseria, G. E., Ernzerhof, M. Hybrid functionals based on a screened coulomb potential. *J. Chem. Phys.* **118**, 8207-8215 (2003).

[5] Krukau, A. V., Vydrov, O. A., Izmaylov, A. F., Scuseria, G. E. Influence of the exchange screening parameter on the performance of screened hybrid functionals. *J. Chem. Phys.* **125**, 224106 (2006).

[6] Monkhorst, H. J., Pack, J. D., Special points for brillouin-zone integrations. *Phys Rev B* **13**, 5188-5192 (1976).